International Journal of Heat and Mass Transfer 143 (2019) 118441

Contents lists available at ScienceDirect

International Journal of Heat and Mass Transfer

journal homepage: www.elsevier.com/locate/ijhmt

Heat transfer, efficiency and turn-down ratio of a dynamic radiative heat exchanger

Rydge B. Mulford, Matthew R. Jones, Brian D. Iverson *

Brigham Young University, Provo, UT 84602, USA

ARTICLE INFO

Article history:
Received 25 February 2019
Received in revised form 24 June 2019
Accepted 17 July 2019

ABSTRACT

Efficient heat transfer is critical in the design and optimization of thermal control systems. Static radiative heat exchangers are often simple and reliable systems but typically cannot be adapted to environmental changes. Adaptable radiative heat exchangers can be adjusted in response to variations in the thermal environment or operating conditions and have the potential for increased efficiency and reduced cost. Dynamic control of a radiative heat exchanger is possible through geometric manipulation of a segmented, self-irradiating fin, consisting of rigid panels that are linked by thermal hinges in an accordion arrangement. In this paper, a numerical model is described to predict the temperature profile and efficiency of a radiative heat exchanger, accounting for conduction and self-irradiation. Governing equations are cast in terms of the conduction-radiation interaction parameter, surface emissivity, actuation angle, and the thermal conductance of the hinges linking the panels. Results indicate that a turn-down ratio (largest possible heat rate divided by smallest possible heat rate) of greater than three is possible for realistic panel geometries and materials. Self-irradiation decreases the turn-down ratio, and there is evidence that an optimal number of rigid panels exists for any combination of panel geometry and device temperature. The maximum efficiency occurs when the plates are in the collapsed position, but the heat rate is at a minimum in this configuration. Finally, the properties and geometry of the plates are shown to have a more significant effect on the turn-down ratio than the properties of the thermal hinges.

1. Introduction

Economical and efficient heat transfer is critical in the design and optimization of thermal control systems. For radiative cooling applications, total cooling power is determined by operating temperature, material properties, and geometry of a dedicated cooling surface. Constraints on component operating temperature typically govern temperature limitations and operating conditions. Likewise, material properties are often constrained by the need for specialized materials and/or surface coatings for specific applications such as spacecraft thermal control [1] or day-time radiative refrigeration [2,3]. Systems that leverage the low-temperature (~3 K) of deep space to efficiently reject heat via radiation have recently been the focus of many researchers [4,5]. These promising radiative cooling technologies require spectrally selective radiative heat exchangers that are engineered to be strongly emitting in the 8–13 μm spectral region and weakly absorbing at wavelengths outside this 'atmospheric window.'

However, it is the *geometry* of dedicated cooling surfaces that is often flexible in addressing increasing power requirements. Although the available emitting surface area of a radiative cooling device may be increased, the size, weight and power requirements of cooling panels must be considered before large surfaces may be utilized, especially with regards to applications such as spacecraft thermal control [6,7]. In particular, radiative heat exchangers used in space are often simple and reliable systems but typically do not adapt to environmental changes. Adjustable systems, that can be adapted for variations in the thermal environment or operating conditions, have the potential for increased efficiency and reduced cost.

As one example, consider a spacecraft in low earth orbit. On this spacecraft, specialized surfaces (radiators) emit waste heat originating from electronics or from solar/albedo irradiation into deep space via thermal radiation. The quantity of waste heat that must be rejected varies in real time as a result of onboard power usage fluctuations and variations in solar and albedo irradiation intensity [1]. However, the emissivity and surface area of the radiator are fixed values, and radiators are designed to function within a narrow band of temperature values [1]. As such, spacecraft radiator surfaces are coated with a high emissivity coating and sized as large as necessary to reject the maximum heat load the spacecraft is expected to experience as the design point. When the spacecraft is generating significant waste heat (i.e. when subjected to full solar irradiation and maximum onboard power usage) the

* Corresponding author.
E-mail address: bdiverson@byu.edu (B.D. Iverson).

https://doi.org/10.1016/j.ijheatmasstransfer.2019.118441
0017-9310/

Nomenclature

α	intrinsic absorptivity
ε	intrinsic emissivity
ε_α	apparent emissivity
$\boldsymbol{\theta}$	temperature profile column vector
θ	non-dimensional temperature
Λ	apparent emissivity correction function
Π_1	heat transfer rate normalized by heat transfer from a straight, black, isothermal fin
Π_2	heat transfer rate normalized by heat transfer from a folded, isothermal fin
σ	Stefan-Boltzmann constant, 5.67×10^{-8} [W m^{-2} K^{-4}]
ϕ	actuation angle, [deg]
χ	non-dimensional panel position
Ψ	turn-down ratio
A	coefficient matrix
b	source term column vector
B_i	Biot number
F	view factor
J	radiosity, [W m^{-2}]
J^*	non-dimensional radiosity
k	thermal conductivity of panel material [W m^{-1} K^{-1}]
κ	hinge thermal conductance [W m^{-2} K^{-1}]
L	panel length, [m]
N	number of finite elements in one panel
N_c	conduction-radiation interaction parameter
N_κ	hinge-conductance radiation parameter
N_p	number of panels in the fin
q'	heat transfer rate per unit depth, [W m^{-1}]
t	panel thickness, [m]
T	temperature of an element, [K]
T_b	temperature of the base, [K]
x	position along the panel length, [m]
Δ_x	length of an element, [m]

Subscripts

cond	heat transfer due to conduction
fin	heat transfer from the entire fin
i	primary element index
in	heat transfer into an element
iso	isothermal
j	radiosity element index
left	radiosity originating from the panel to the left of the element
n	panel index
out	heat transfer leaving an element
rad	heat transfer due to radiation
right	radiosity originating from the panel to the right of the element

Superscripts

k	iteration number

radiators operate at this design point. However, when spacecraft waste heat drops below the maximum value, the radiators emit an excessive amount of heat. Such behavior may cause the temperature of components aboard the spacecraft to fall below established survival limits; therefore, onboard heaters are activated to warm the spacecraft components so that they function within operating limits. This methodology is often referred to as cold-biasing and it has been utilized since the early days of space exploration. However, cold-biasing requires heaters, thermostats, additional battery capacity and additional solar panel capacity to be placed aboard the spacecraft, accounting for approximately 10% of the spacecraft's weight budget. Likewise, the heaters consume upwards of 10% of the spacecraft's total power budget at full power [1]. Traditional satellites, the International Space Station (ISS) and a new class of low-cost, low-risk satellites (e.g. CubeSats) are each designed with this cold-biasing approach.

Recent technology developments [8–10] propose the use of origami-inspired structures, consisting of small, rigid sections connected in a tessellated pattern, to collapse large radiating surfaces into a stowable volume. Intrinsic to this technology is the capability for control of radiative heat transfer via manipulation of surface geometry in real-time. The operating mechanism of these surfaces is such that both the apparent radiative properties of the device [11,12] as well as the apparent emitting surface area of the device [9] vary as a function of deployment position. The net effect is that the total radiative cooling power tends to decrease as the tessellated surface collapses into the stored state while deploying the surface into a fully-actuated state increases the total cooling power [9]. By controlling the position of the origami structure, the radiative cooling power of the radiative heat exchanger may be adjusted to real-time system requirements.

Published studies concerning the radiative behavior of origami tessellations have been limited to isothermal surfaces, neglecting heat conduction. However, the series of panels comprising the tessellation naturally forms a segmented radiative fin that is self-irradiating (Fig. 1). A number of researchers have evaluated arrays of mutually irradiating stationary fins consisting of cylindrical, rectangular or triangular fins connected to a common planar or cylindrical base [13–19] as well as single conical or fractal-like fins that are self-irradiating [20,21]. Many of these studies report fin efficiency as a function of fin design parameters and optimize the dimensions of the fin or fin array. However, the thermal performance of a self-irradiating fin with dynamic geometry has yet to be considered.

A radiative fin array is likely preferable to a single large radiative fin for achieving the greatest heat transfer per unit mass for a given base temperature. However, a radiative fin array is not always possible. As an example, CubeSat spacecraft architectures usually do not include external surfaces designed for radiative heat exchange as all available external panel surfaces are typically covered in solar panels [22]. A deployable radiative fin would provide radiative surface area that is easily stowed on board and then deployed upon launch. As an added benefit, the folded nature of the radiative fin then provides the opportunity for dynamic control of the radiative fin geometry to optimize heat transfer behavior.

In this study, the turn-down ratio (ratio of largest to smallest radiative heat loss) and efficiency of a segmented, dynamic, radiative heat exchanger (consisting of multiple, mutually irradiating straight segments arranged in series, forming a self-irradiating actuating fin) is described as a function of surface radiative properties and static/dynamic dimensions. This work considers the accordion tessellation, a repeating structure of V-grooves, as this geometry bears the strongest resemblance to static spacecraft radiators deployed at orbit insertion on the International Space Station [23] and other commercial and scientific satellites [24–27] as well as to dynamically-actuated radiators currently in development [7,28,29]. The accordion fold has also been explored for solar shading applications of buildings [30]. However, the numerical approach detailed in this paper, which is designated as the Segmented Fin Algorithm (SFA), may be applied to other two-dimensional tessella-

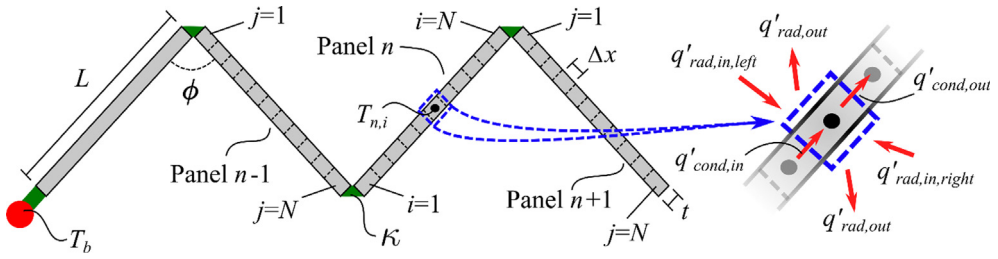

Fig. 1. Geometry of a re-deployable, segmented fin connected to a base (at T_b) consisting of several rigid straight panels that are connected in series via thermally conductive hinges. The apparent surface area and apparent radiative properties of the fin vary as the fin is actuated.

tions of interest. The 2D approach in this work is also applicable to three-dimensional tessellations considered viable for spacecraft missions, such as the flasher [31,32] or square patterns, if the depth to panel length ratio is sufficiently large [10]. Surfaces are assumed to exhibit diffuse reflection in the present study, and fin geometries are restricted to isothermal conditions across the panel thickness. In order to focus the results of the paper on the fundamental radiative behavior of a dynamic radiative fin geometry, the influence of radiative sources aside from the fin geometry (such as spacecraft surfaces, building rooftops, solar inputs, etc.) are not considered in this work and may be incorporated by those using the approach outlined here. Regardless, excluding external radiative sources can be an appropriate assumption for select applications, including long, cantilevered radiators extending away from a co-planar spacecraft (e.g. ISS, CubeSats).

First, the governing equation of the numerical model is presented, including non-dimensionalization of the design variables and comparison metrics of interest. The numerical solution approach used to determine an accurate temperature profile of the dynamic radiative fin is described and limiting conditions are defined. Simulation results are compared with available analytical solutions for a static, rectangular radiative fin and for an isothermal V-groove to verify the performance of the model and code. Results of the numerical model are described and the influence of the actuation position, number of tessellation panels, surface emissivity, conduction-radiation interaction parameter, and hinge-conductance radiation parameter on the temperature profile, heat transfer, efficiency, and turn-down ratio of the device is described. Finally, results are further discussed in light of application considerations.

2. Methodology

2.1. Segmented fin algorithm

2.1.1. Model geometry

A rigid, straight panel of known thermal conductivity (k), surface emissivity (ε), thickness (t), and length (L) having a unit width in-and-out of the page is connected to an isothermal base (T_b) via a flexible thermal hinge with a given thermal conductance (κ, reported per unit area). At the tip of the base-mounted panel, an additional thermal hinge, also of thermal conductance κ, connects the tip of the first panel to the base of another straight, rigid panel (Fig. 1). This repeating behavior continues for N_P panels, where the geometric angle between two adjacent panels is identical across the entire series and specified as the actuation angle (ϕ). The resulting pattern of angled panels forms an accordion tessellation, resulting in a self-irradiating, segmented, radiative fin.

2.1.2. Governing equation

Each panel is discretized into N number of finite, isothermal elements which include the entire thickness of the radiator panel and with uniform finite length (Δx). The geometric center of each element contains a node at a certain temperature, designated as $T_{n,i}$, where n is the panel index (as numbered from the base) and i is the index of the element (as numbered from the base-side of the panel) as shown in Fig. 1.

Consider an energy balance on a single element (Eq. (1), inset Fig. 1). Heat enters this element via one-dimensional conduction from the left element (n, $i-1$) and leaves via conduction to the right element (n, $i+1$); both conduction terms may be described with Fourier's Law at the element boundary (Eq. (2)). To allow for numerical calculation, the temperature gradient in Fourier's Law is replaced with a finite difference approximation between adjacent temperature nodes (right-hand-side of Eq. (2)), where the distance between nodes is equivalent to the length of an element, Δx. Energy leaving the element via conduction is determined in a similar manner.

$$q'_{cond,in} - q'_{cond,out} + q'_{rad,in,left} + q'_{rad,in,right} - q'_{rad,out} = 0 \tag{1}$$

$$q'_{cond,in} = -kt\frac{dT}{dx} \approx kt\frac{T_{n,i-1} - T_{n,i}}{\Delta x} \tag{2}$$

Radiant energy is incident on the element from the left ($q'_{rad,in,left}$) and right ($q'_{rad,in,right}$) panels as well as emitted from both sides of the element (c). The rate at which radiant energy from an element on the left panel ($n-1, j$) is absorbed by element n, i is determined by multiplying the absorptivity of the panel surface, radiosity of the left element, view factor between the two elements, and the area of the left element, or $\alpha J_{n-1,j}F_{j-i}\Delta x_j$, assuming diffuse and gray surfaces. The heat originating from the entire left panel that is absorbed by element n,i is determined by summing over all elements on panel $n-1$ as shown in Eq. (3), where N represents the total number of elements on an individual panel, where all panels have the same number of elements. The absorbed heat from the right panel ($q'_{rad,in\ right}$) is given by a similar expression, where the index j now indicates elements on the panel n + 1 and $J_{n-1,j}$ is replaced with $J_{n+1,j}$. The heat emitted from the element is given by Eq. (4), which accounts for emission from both exposed surfaces.

$$q'_{rad,left,in} = \alpha\sum_{j=1}^{N} J_{n-1,j}F_{j-i}\Delta x_j \tag{3}$$

$$q'_{rad,out} = 2\varepsilon\sigma\Delta x_i T_{n,i}^4 \tag{4}$$

After substituting Eqs. (3) and (4) into the energy balance, the governing equation becomes,

$$kt\frac{T_{n,i-1} - T_{n,i}}{\Delta x_i} - kt\frac{T_{n,i} - T_{n,i+1}}{\Delta x_i} + \alpha\sum_{j=1}^{N} J_{n-1,j}F_{j-i}\Delta x_j + \alpha\sum_{j=1}^{N} J_{n+1,j}F_{j-i}\Delta x_j - 2\varepsilon\sigma\Delta x_i T_{n,i}^4 = 0 \tag{5}$$

Emission and reflection from the base geometry to which the dynamic radiative fin is attached as well as irradiation from the surroundings have been shown to impact the heat transfer behav-

ior of a parallel radiative fin array [13,33]. However, these influences were not considered in this work for two reasons. First, the focus of this paper is the fundamental heat transfer behavior of a dynamic radiative fin, focusing on the impact of self-irradiation on the fin heat transfer and temperature profiles. As such, external inputs were not considered in order to focus on the basic behavior. Second, it is difficult to identify and generalize the exact geometry of the base and the strength and directionality of radiation from the surroundings. Instead the influence of these factors on the heat transfer and temperature profiles of self-irradiating dynamic fins is left as future work. Finally, there are application scenarios where external inputs (specifically from the base) are negligible, including heavily insulated spacecraft or spacecraft with geometry such that the fin panels do not view the spacecraft significantly.

Likewise, the use of a 2D model results in error when used to predict the performance of 3D surfaces. As real radiative fins are three dimensional, it is necessary to ensure that panels of sufficient depth are used such that the infinite depth assumption does not introduce significant error. It has been shown that 3D V-grooves with a depth to panel length (L) ratio of 10 or more exhibit radiative heat transfer values within 95% of the values predicted by a 2D model [10]. Results provided in this work are best applicable to self-irradiating, segmented fins that meet this criteria. The approach established here may be extended for other 3D surfaces.

The governing equation is non-dimensionalized using the terms given in Eqs. (6)–(9). The local temperature T is scaled by the temperature of the base T_b; the element length Δx is scaled by the length of a single panel L; the thermal conductivity, panel length, panel thickness and base temperature are combined to form the radiation-conduction interaction parameter (N_c), being a ratio of the resistance to conduction through the fin material to the resistance to radiation heat transfer from the fin surfaces, where this non-dimensional term is often utilized in radiative fin solutions [13]; the radiosity J is scaled by the emissive power of the base σT_b^4.

$$\theta = \frac{T}{T_b} \tag{6}$$

$$\chi = \frac{x}{L} \tag{7}$$

$$N_c = \frac{R_{cond}}{R_{rad}} = \frac{\sigma T_b^3 L^2}{kt} \tag{8}$$

$$J^* = \frac{J}{\sigma T_b^4} \tag{9}$$

The intrinsic emissivity and intrinsic absorptivity are equivalent in this work as the surfaces are assumed to be diffuse and gray. Likewise, the intrinsic radiative properties of the surface were not included in non-dimensional terms in order to explore their specific effect on the heat transfer and turn-down ratio of a self-irradiated, segmented fin.

The non-dimensional form of the governing equation for an internal element is given as Eq. (10) after recalling that all elements have an equivalent length $\Delta\chi$. The view factor F used in this analysis is for exchange between finite areas on one side of a V-groove to another as reported in the Hottel crossed strings section in Modest [34] or condition A-10 in the configuration catalog [35].

$$\frac{1}{\varepsilon\Delta\chi^2 N_c}\left[-2\theta_{n,i}+\theta_{n,i-1}+\theta_{n,i+1}\right]+\sum_{j=1}^{N}J^*_{n-1,j}F_{j-i}+\sum_{j=1}^{N}J^*_{n+1,j}F_{j-i}-2\theta^4_{n,i}=0 \tag{10}$$

Elements found on the ends of the radiator panels, having an index $i = 1$ or $i = N$, will be subject to different boundary conditions than an interior node and therefore require a modified form of Eq. (10). The first element ($i = 1$) on any panel is connected to the last element of the previous panel, or the base in the case of the first panel, using a thermal hinge with thermal conductance κ. Conduction terms across these thermal hinges (e.g. $q'_{cond,in}$ in Eq. (1)) can be described using Eq. (11). For the last element on a panel ($i = N$), Eq. (11) is modified by replacing subscript $n-1$ with n and subscript n with $n+1$; these modified forms are then substituted into the term $q'_{cond,out}$ found in Eq. (1).

$$q'_{cond,in} = \kappa t(T_{n-1,N} - T_{n,1}) \tag{11}$$

The governing equation for these boundary elements is non-dimensionalized in the same manner as Eq. (10). However, the thermal conductance κ is non-dimensionalized to obtain a hinge-conductance radiation parameter $N\kappa$ (Eq. (12)), similar to the conduction-radiation interaction parameter but with one length scale now incorporated into the conductance. This parameter N_κ is a ratio of the resistance to conduction through the hinge and the resistance to radiative heat transfer from the panel surfaces. The last element of the last panel is assumed to be insulated at the tip.

$$N_\kappa = \frac{R_{cond,hinge}}{R_{rad}} = \frac{\sigma T_b^3 L}{\kappa t} \tag{12}$$

Substituting Eq. (11) into Eq. (1) and proceeding as was done for an internal node, the non-dimensional form of the governing equation for the first element on a panel ($i = 1$) is given by Eq. (13). The governing equation for an element on the end of a panel ($i = N$) is given in Eq. (14).

$$\frac{1}{\varepsilon\Delta\chi N_\kappa}(\theta_{n-1,N}-\theta_{n,1})+\frac{1}{\varepsilon\Delta\chi^2 N_c}(\theta_{n,2}-\theta_{n,1})+\sum_{j=1}^{N}J^*_{n-1,j}F_{j-1}+\sum_{j=1}^{N}J^*_{n+1,j}F_{j-1}-2\theta^4_{n,1}=0 \tag{13}$$

$$\frac{1}{\varepsilon\Delta\chi^2 N_c}(\theta_{n,N-1}-\theta_{n,N})+\frac{1}{\varepsilon\Delta\chi N_\kappa}(\theta_{n+1,1}-\theta_{n,N})+\sum_{j=1}^{N}J^*_{n-1,j}F_{j-N}+\sum_{j=1}^{N}J^*_{n+1,j}F_{j-N}-2\theta^4_{n,N}=0 \tag{14}$$

Mathematical closure for Eqs. (10), (13), or (14) is obtained with the definition of the radiosity for each exposed side of an element. The radiative heat rate leaving element i per unit depth is defined in Eq. (15). This equation includes the emission from element i summed with the reflected portion of energy incident from opposing elements, being the product of element j's radiosity, view factor to element i, and length (Δx_j) summed over all elements on the opposing panel. The length of every element is identical, causing element length terms to cancel and giving the definition of the radiosity for the element surface facing the right panel ($n+1$) in Eq. (16) and non-dimensionalized in Eq. (17). For the side of the element facing the left panel ($n-1$), the radiosity is still given by Eq. (17) although the subscript of J^* must be changed to $n-1$. When one side of the element only experiences radiative heat exchange with the surroundings (e.g. the top surface of panel 1 or panel 4 in Fig. 1 or when the panels are flat, $\phi = \pi$), the dimensionless radiosity reduces to only the first term of Eq. (17).

$$J_{n,i}\Delta x_i = \varepsilon\Delta x_i\sigma T^4_{n,i} + (1-\alpha)\sum_{j=1}^{N}J_{n+1,j}F_{j-i}\Delta x_j \tag{15}$$

$$J_{n,i} = \varepsilon\sigma T^4_{n,i} + (1-\alpha)\sum_{j=1}^{N}J_{n+1,j}F_{j-i} \tag{16}$$

$$J^*_{n,i} = \varepsilon\theta^4_{n,i} + (1-\alpha)\sum_{j=1}^{N} J^*_{n+1,j}F_{j-i} \tag{17}$$

2.1.3. Solution method

A balance equation is written for every element on each panel. This series of equations is cast into matrix form as shown in Eq. (18), where **A** is a square matrix with n × N rows and n × N columns containing the coefficients for the linear non-dimensional temperature variables, θ is a column vector with n × N entries containing the unknown temperature profile, and **b** is an n × N column vector containing the source terms, being the radiosity summation terms as well as the nonlinear thermal emission term ($2\theta^4$).

$$\mathrm{A}\theta = b \tag{18}$$

A and **b** are built sequentially, beginning with the first element of the first panel and iterating along *i* and *n*. The row number of **A** and **b** corresponding to element *i* of panel *n* is given by the expression $(n-1)N+i$**.** Coefficients in the first row of **A** and **b**, corresponding to the first element of the first panel, are generated using Eq. (13) where the term $\theta_{n-1,N}$ is the temperature of the base, θ_b. For the remaining elements, if the row number divided by *N* is a whole number, indicating an element immediately to the left of a hinge, then Eq. (14) is used to determine coefficients for **A** and **b**. Likewise, if the row number divided by $(N-1)$ is a whole number, indicating an element to the right of a hinge, then Eq. (13) is used to generate coefficients for **A** and **b.** All other rows utilize Eq. (10). The last row of **A** and **b**, being row n × N, corresponds to the last element of the last panel and is determined using Eq. (14) but with the second variable grouping $(\theta_{n+1,1} - \theta_{n,N})$set to zero, giving an insulated tip.

The presence of a non-linear temperature term as well as temperature-dependent radiosity terms within the source term vector necessitates an iterative process in order to converge to the correct temperature profile. To proceed, an initial guess of the temperature profile is made and the radiosity profiles of the top and bottom surface of each panel are assumed, allowing the source vector to be calculated. For all tests in this work, the initial temperature profile was guessed to be isothermal and equal to the base temperature and with initial radiosity values defined using only the first term of Eq. (17). The matrix system found in Eq. (18) is then solved using the calculated source vector, giving a new temperature profile. The temperature for every element in the new temperature profile is compared with its equivalent in the guessed temperature profile. If the difference between the two profiles exceeds a specified convergence criterion, then the source vector is recalculated and a new temperature profile is obtained. This procedure is repeated until the convergence criterion of $\theta^{k-1}_{n,i} - \theta^{k}_{n,i} = 1\times10^{-5}$ is met, where the superscript *k* indicates the iteration number. To recalculate the source vector using a new temperature profile the radiosity profiles must first be updated. Beginning at the first element on the first panel and moving towards the end of the fin, the radiosity profile at each node is updated individually using Eq. (17) for an element surface facing the panel to the right or a modified form of Eq. (17) for an element surface facing the panel to the left, utilizing the updated temperature profile and the most recently available radiosity information.

The iterative procedure just described requires frequent recalculation of updated temperature profiles through solution of the matrix equation given in Eq. (18). By using a linear approximation to estimate the conduction terms, as shown in Eq. (2), coefficients for a given row in the **A** matrix only pertain to the current element (the coefficients found on the matrix diagonal) as well as the two elements immediately adjacent. As such, the **A** matrix is tri-diagonal and the system is solved with simplified Gaussian elimination using the Tri-Diagonal Matrix Algorithm (TDMA) as described in [36].

2.2. Verification

2.2.1. Grid independence study

The accuracy of the converged temperature profile is dependent on the length of the element, given non-dimensionally as $\Delta\chi$. To ensure an accurate solution for all tested cases, a grid refinement study was performed for the extremes in the variables; these include combinations of the smallest (1×10^{-5}) and largest (10) N_c values with the smallest (0.1) and largest (0.9) intrinsic emissivity values. For each combination, an initial element size was selected and the iterative temperature profile solution process was executed. Upon solution, the element size was decreased by a factor of two and a new temperature profile was determined, starting with the most recent temperature profile as an initial guess. The temperature profiles were compared and the process was repeated until the difference between the iterated temperature profiles for all elements fell within the bounds of an overall convergence criteria. For this study, the overall convergence criteria was$\theta^{k-1}_{n,i} - \theta^{k}_{n,i} = 1\times10^{-3}$ resulting in 2000 elements per panel (*N*) to satisfy the grid independence criterion for all four tested cases. All data points in this study were conducted with *N* = 2000.

2.2.2. Limiting condition

In developing the self-irradiating fin model, the temperature at any position on any panel was assumed to be isothermal through the thickness of the panel. When applied to a given geometry, this assumption must be validated using the Biot number to ensure accuracy. Using the radiation heat transfer coefficient obtained by linearizing the radiation rate equation [37] with surroundings at a temperature of 0 K and assuming the characteristic conduction length to be the thickness of the material, the Biot number of the element is given as Eq. (19).

$$Bi = \frac{\varepsilon\sigma T_b^3 t}{k} = \frac{N_c\varepsilon t^2}{L^2} \tag{19}$$

This number compares radiative emission from the surface with conduction through the thickness. To be conservative, the Biot number analysis given as Eq. (19) ignores radiative energy absorbed by the element and the highest temperature, T_b, should be used. Results for the Biot number for a particular application as calculated in this manner should be less than 0.1 to ensure appropriate application of the isothermal condition through the thickness of the panel. Results presented in this paper are provided in terms of non-dimensional parameters, without selection of specific values for *t,* ε and *L*; the condition of a small Biot number should be verified before applying these results to a particular application.

2.2.3. Model validation

To test the accuracy of the SFA, numerical results using the current approach are compared with known analytical solutions for certain idealized cases. First, the actuation angle is defined as 180° and the hinge-conductance radiation parameter is set to $\Delta\chi N_c$, resulting in a flat, straight fin of homogeneous material. The solution provided by the SFA for this scenario corresponds with the analytical solution for a straight rectangular radiating fin with negligible base interactions (available from [38], repeated in Eq. (20)).

$$x = \left(\frac{5kt}{4\varepsilon\sigma}\right)^{1/2}\int_{T}^{T_b}\frac{dT}{\left[T^5 - T^5_{L\cdot N_p} - (5/2\varepsilon\sigma)(T - T_{L\cdot N_p})\right]^{1/2}} \tag{20}$$

To evaluate this expression, the temperature at the end of the fin is first evaluated by setting $x = L{\cdot}N_P$ (the total length of the fin) and determining the correct T that satisfies the integral with root-finding methods so that the temperature at the tip of the fin can be obtained. A temperature value is then chosen between the tip temperature and base temperature. Eq. (20) is evaluated by integrating from the selected temperature to the base temperature, giving the x location for the selected temperature. A new temperature value is selected and its associated x value is determined with Eq. (20). This process is repeated until a sufficient number of points have been evaluated and the temperature profile of the fin is clear. Comparison of the temperature profiles using the current method and the analytical solution are provided in the results.

To test the accuracy of the radiative interactions, the emissivity of the surface is set to 0.3, the conduction-radiation interaction parameter is set to zero (e.g. a fin with infinite thermal conductivity) and the hinge-conductance radiation parameter is set to $\Delta\chi N_c$. The heat loss from one V-groove of the resulting isothermal fin with an emissivity of 0.3 is calculated for all actuation angles and this value is divided by the heat loss from a black V-groove of the same geometry to determine the apparent emissivity [12] as calculated by the SFA. The resulting apparent emissivity value is compared with a correlation from ray tracing data for the apparent emissivity of an isothermal V-groove [11] as given in Eqs. (21) and (22), where the variable Λ is the apparent emissivity correction function.

$$\varepsilon_a = \varepsilon\Lambda\sum_{m=0}^{\infty}(1-\varepsilon)^m\left[1-\sin\left(\frac{\phi}{2}\right)\right]^m \tag{21}$$

$$\Lambda = 1-[0.0169-0.1900\ln(\varepsilon)]\exp\left(-1.4892\varepsilon^{-0.4040}\phi\right) \tag{22}$$

2.3. Result metrics

The SFA outputs the non-dimensional temperature distribution of the segmented fin and the non-dimensional radiosity distributions for the top and bottom fin surfaces. In order to study the effect of the parameters ε, N_c, N_P, and $N\kappa$ on the heat transfer performance of the fin, several metrics are proposed. The first of these metrics is the fin heat transfer rate non-dimensionalized using the maximum possible radiative transfer from the fin (Π_1). To determine this value, the heat transfer per unit width across the thermal hinge (Eq. (11)) is applied to the first hinge and scaled using the total emission per unit width leaving a straight, black, isothermal radiative fin having the same length as a fully extended segmented fin, as shown in Eq. (23).

$$\Pi_1 = \frac{q'_{fin}}{2LN_P\sigma T_b^4} = \frac{1-\theta_{1,1}}{2N_\kappa N_P} \tag{23}$$

Here, $\theta_{1,1}$ is the non-dimensional temperature of the first node of the first panel and Π_1 is the non-dimensional fin heat transfer rate. The non-dimensional fin heat rate is defined as the ratio of the heat rate through the fin to the heat rate through a black, fully-extended, isothermal fin of the same dimensions. The non-dimensional fin heat rate reports a relative heat transfer value and is used to determine how the heat transfer of the dynamic segmented fin varies with actuation and is a measure of how efficiently the mass of the fin is being utilized. This term is referred to as the "non-dimensional heat transfer" throughout the remainder of this work.

A second non-dimensional heat transfer value is used in this work in order to examine the heat transfer behavior of a dynamic segmented radiative fin. This heat transfer value is calculated by dividing the heat rate of the segmented fin calculated using Eq. (11) by the heat rate of the same segmented fin with an isothermal temperature profile for the same intrinsic emissivity and actuation angle. The heat loss of the isothermal fin is the summation of the emission from the V-groove cavity openings, utilizing the apparent emissivity (Eqs. (21) and (22)) and the emission from the panel surfaces that are exposed only to the isothermal surroundings Eq. (24); Eq. (11) is not used to find the heat loss from an isothermal fin as this equation would return a value of zero in the isothermal case. This second non-dimensional heat transfer value quantifies how closely the fin temperature profile approaches isothermal conditions and therefore indicates how effectively heat is being transferred along the length of the fin. This metric resembles the classic definition of fin efficiency and will therefore be referred to as "fin efficiency" throughout the remainder of this work.

$$\Pi_2 = \frac{q'_{fin}}{q'_{fin,iso}} = \frac{\theta_b-\theta_{1,1}}{2N_\kappa\left[\varepsilon+\varepsilon_a(N_P-1)\sin\left(\frac{\phi}{2}\right)\right]} \tag{24}$$

Finally, the turn-down ratio (Ψ) is defined as the ratio of the largest possible non-dimensional fin heat rate to the smallest possible non-dimensional fin heat rate (using Eq. (23)) over the full range of actuation angles while ε, N_c and $N\kappa$ are held constant. For this work, the turn-down ratio was determined by dividing Π_1 evaluated at an actuation angle of 180° by Π_1 evaluated at an actuation angle of 5° (the smallest angle considered). A larger turn-down ratio indicates an increased range of radiative heat transfer control.

3. Results and discussion

3.1. Verification comparisons

Fig. 2a plots the non-dimensional temperature profile against the non-dimensional, length-wise panel coordinate χ for both the SFA and the analytical results from Eq. (20). Results are provided for four different values of N_c and an intrinsic emissivity value of 0.90. Given the definition of χ as shown in Eq. (7), whole number values of χ represent the location of thermal hinges between adjacent panels. As seen in Fig. 2a, SFA results are in excellent agreement with the analytical results, with slight disagreement apparent when χ, N_c and ε are large. For $0.005 \le N_c \le 10$ and $0.1 \le \varepsilon \le 0.9$, the largest discrepancy between the SFA temperature profile and the analytical temperature profile is 3%. For these cases, the temperature profile becomes less accurate as χ increases. Since these discrepancies are negligibly small, comparison of the analytical and SFA results verifies the conduction and emission portions of the code.

To verify the behavior of re-reflected energy within the V-grooves, the SFA results for an isothermal fin are compared in Fig. 2b with an apparent emissivity correlation given in Eqs. (21) and (22) over the full range of actuation angles for an intrinsic emissivity of 0.3. The average relative discrepancy between the SFA and correlation is 2% for $0.1 \le \varepsilon \le 0.9$ (step size of 0.1) over the full range of cavity angles. Perfect agreement between the SFA and correlation is not expected due to uncertainty inherent to the correlation, with correlation uncertainty approaching 1.6% for actuation angles near 0°. Since the largest SFA/correlation discrepancy is comparable to the uncertainty in the correlation and also occurs near angles of 0°, the ability of the SFA to correctly predict radiosity is considered verified.

3.2. Large thermal hinge conductance

Results are first presented for the case where conduction resistance across the thermal hinge is negligible ($N\kappa = \Delta\chi N_c$), representing a single continuous material that has been folded into an accordion pattern with an isothermal boundary condition on one end. When a value of $N\kappa = \Delta\chi N_c$ is used, governing equations for

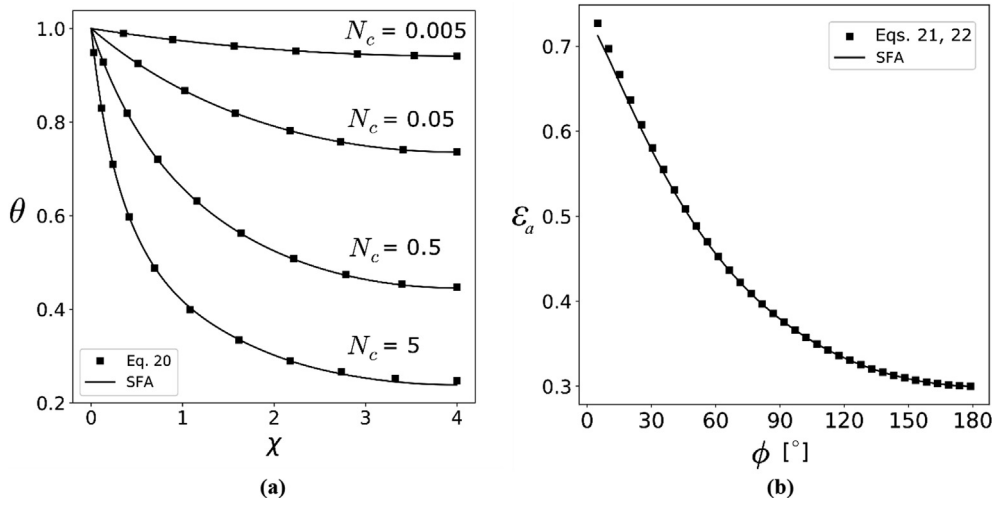

Fig. 2. **(a)** Results of the Segmented Fin Algorithm (SFA) compared with results from an analytical, straight, radiative fin solution (Eq. (20)) for $\varepsilon = 0.90$. The numerical algorithm agrees well with the analytical approach with a largest relative error of 3%, obtained at large values of N_c, ε, and χ. **(b)** The apparent emissivity of a V-groove (ε_a) as calculated using the SFA compared with a published correlation (Eqs. (21) and (22)). The largest error between the SFA and correlation is 2% which is similar to the range of errors given for the correlation.

the first or last element on a panel, given by Eqs. (13) and (14) respectively, are transformed into the governing equation for an element in the middle of the panel as given by Eq. (10). This scenario explores the operation of a deployable fin without the added complexity of a hinge resistance. Fig. 3a displays the temperature profile for a four-panel, hinged radiator with an intrinsic emissivity of 0.9 and conduction-radiation interaction parameters of 0.05 or 10. Results are displayed for four different actuation angles, ϕ = 5°, 30°, 90°, 150°. Fig. 3b gives temperature profiles for these same N_c values, actuation angles, and number of panels but for an intrinsic emissivity of 0.1.

For small N_c values, indicated by the family of curves labeled $N_c = 0.05$ in Fig. 3a and 3b, conduction dominates inter-panel heat exchange over radiation. As such, the temperature drop from the base to the tip of the fin is small when compared with temperature profiles for fins with large N_c values. Likewise, the influence of self-irradiation on the fin temperature profile is evident in the changing tip temperature of the fin with changes in actuation angle. However, temperature profiles for all angles still approximate an exponentially decaying form except for slight perturbations in the middle two panels ($1 < \chi < 3$) for small actuation angles. Regarding emissivity, the fin with a high emissivity experiences a 5x larger reduction in tip temperature than for a fin with low emissivity when comparing tip temperatures in the fully extended and fully collapsed positions.

At large N_c values (e.g. $N_c = 10$ curve families in Fig. 3a and 3b), radiative losses dominate inter-panel heat exchange over conduction. As such, self-irradiation causes significant variation in the temperature profile as compared to the exponentially-decaying straight-fin temperature profile given approximately by $\phi = 150°$. For large emissivities, the temperature of the second panel ($1 < \chi < 2$) can be seen to *increase* as χ increases, especially for small actuation angles, indicating that heat is conducted *towards* the base of the fin. Although counter-intuitive, this behavior may

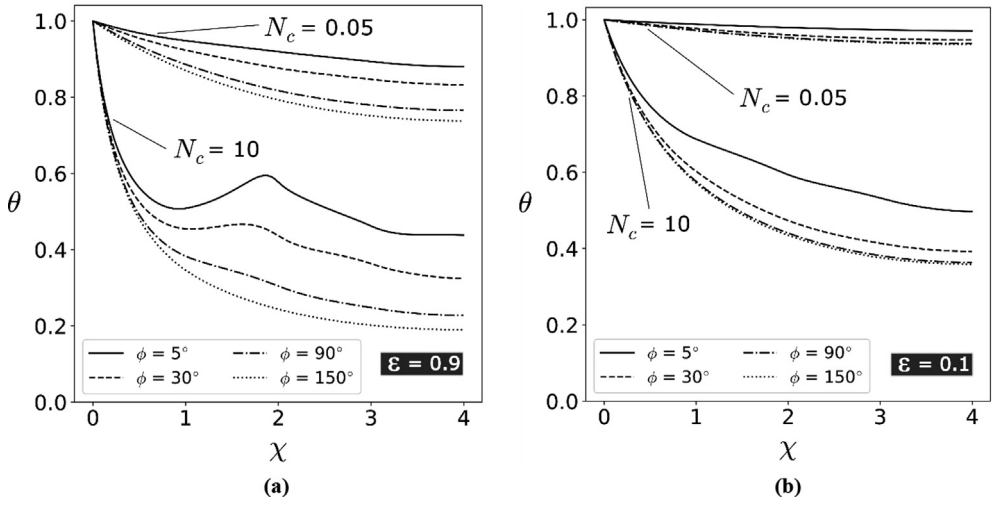

Fig. 3. Non-dimensional temperature (θ) profiles as a function of non-dimensional panel position (χ) for a four-panel, hinged radiator at two values of the conduction-radiation interaction parameter (N_c). Results are displayed for increasing values of the actuation angle (ϕ), showing the influence of fin deployment position on the temperature profile. **(a)** Behavior observed for an intrinsic emissivity of 0.9. When conduction dominates ($N_c < 1$), the profile approximates that of a straight radiative fin. When radiation dominates ($N_c > 1$) the influence of radiative exchange between panels causes significant variation in the panel temperature profiles. **(b)** Behavior observed for an intrinsic emissivity of 0.1. As a result of the nearly reflective surface, conduction dominates inter-panel heat exchange and the profiles continuously decrease as χ increases.

be explained with an examination of the fin's geometry. For very small actuation angles ($\phi < 5°$), the hottest elements at the beginning of the first panel ($0 < \chi < 0.25$) are within close radiative proximity to the elements at the end of the second panel ($1.75 < \chi < 2$), resulting in significant radiative transfer from the beginning of the first panel to the end of the second panel. This elevated radiative transfer combined with the weak influence of conduction generates a local hot spot near the end of the second panel, causing heat to conduct away from this location in both the $+\chi$ and $-\chi$ directions. However, for reflective surfaces ($\varepsilon = 0.1$), the effect of radiative heat transfer is decreased, resulting in monotonically decreasing temperature profiles for all cases (see Fig. 3b). The tip temperature reduces in value as actuation angle increases for both emissivities.

Fig. 4a illustrates the non-dimensional heat transfer (Π_1) of the dynamic fin as a function of actuation angle ϕ for an emissivity of 0.9 and Fig. 4b displays this same information for an emissivity of 0.1. Universally, the heat transfer increases as the actuation angle increases, although this change reduces in value as N_c increases. For nearly black surfaces, the heat transfer curves follow an approximate sine distribution, indicating that the heat loss is dominated by the surface area of the V-groove openings, which increase along a sine distribution with angle. However, as the intrinsic emissivity decreases, the heat transfer variation becomes increasingly concentrated towards the small angle range (see Fig. 4b), suggesting that inter-reflections (which are significant in the small angles) dominate the total heat transfer. Finally, smaller N_c values result in more significant heat transfer control, where a nearly black surface with an N_c value of 10 shows only a 3% variation in heat transfer over the full actuation angle range.

Fig. 4a and 4b also display the fin efficiencies (Π_2) for high and low emissivity fins, respectively. Universally, the efficiency of a dynamic fin decreases as the fin actuates from a collapsed to an extended state, indicating that the fin temperature profile is deviating further from isothermal conditions. This behavior is the result of conduction and radiation acting simultaneously when the fin is collapsed to move energy along the fin in the positive χ direction, causing the fin tip temperature to increase and improving fin efficiency. The influence of self-irradiation decreases significantly as the actuation angle increases, causing the fin efficiency to drop with actuation. Regarding emissivity, a reflective fin is always more efficient for all actuation angles when compared with a nearly black fin with an equivalent N_c value. Finally, it is interesting to note that the largest variation in fin efficiency with actuation does not occur at the lowest or highest N_c but is found to exist, for all emissivities, at an optimal value of N_c found between the extremes.

The turn-down ratios (Ψ) for fins with four panels and intrinsic emissivities of 0.9 or 0.1 as a function of N_c are shown in Fig. 5a. Large values of N_c result in turn-down ratios near unity regardless of emissivity, indicating a device with very little capability for radiative heat transfer control. As N_c decreases the turn-down ratio increases and then asymptotes to a limiting value. For a nearly black fin ($\varepsilon = 0.9$) with four panels, the asymptotic value for Ψ is 3.48. For a reflective surface ($\varepsilon = 0.1$) the asymptotic value is 2.43. The inset of Fig. 5a illustrates the behavior of turn-down ratio as a function of intrinsic emissivity for an N_c value of 0.001, where turn-down ratio increases logarithmically as a function of emissivity. Fig. 5b plots the turn-down ratio for a dynamic fin with nearly-black ($\varepsilon = 0.9$) panels as a function of the number of panels (N_P) for four different N_c values. As expected, increasing the total deployed surface area by increasing the number of panels will generally increase turn-down ratio. However, this increase in turn-down ratio will eventually reach a maximum and then decrease as the number of panels increases.

3.3. Finite thermal hinge conductance

Results are now presented for the case when $N\kappa$ is non-zero, indicating the presence of a flexible thermal hinge. Fig. 6a displays the temperature profile of a nearly black ($\varepsilon = 0.9$) dynamic fin having four panels with an N_c value of 0.01 as a function of non-dimensional panel position for actuation angles of 5°, 90°, and 150° and for three different values of $N\kappa$, being 0.01, 0.5, and 10. The hinge thermal conductance value (κ) captures the influence of hinge thermal conductivity, geometry, and thermal interface losses in a single value. Although convenient, this method does not allow for the determination of the temperature profile within the hinge itself resulting in apparent temperature discontinuities (as shown in Fig. 6a) representing the total temperature change across the thermal hinges.

Fig. 6a displays temperature profiles for the case when conduction dominates radiation ($N_c = 0.01$). When $N\kappa$ and N_c are on the same order of magnitude, the temperature drop across thermal

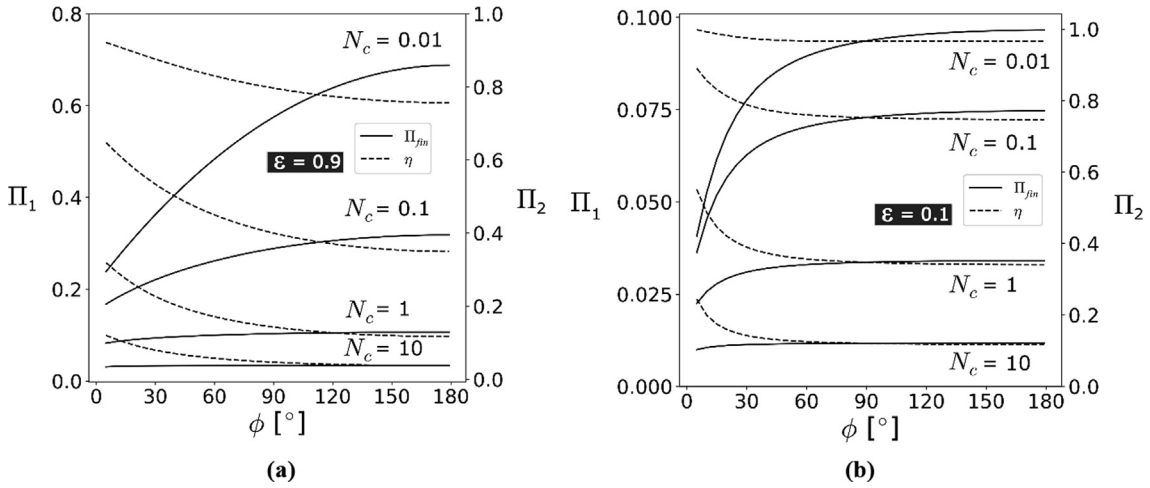

Fig. 4. Non-dimensional fin heat transfer (Π_1) and fin efficiency (Π_2) as a function of actuation angle (ϕ) for four different values of the conduction-radiation interaction parameter (N_c). **(a)** Behavior observed for an intrinsic emissivity of 0.9. The greatest variation in heat transfer is seen for fins where conduction dominates and heat transfer varies significantly over the full actuation angle range. Fin efficiency decreases as the fin extends towards an open configuration. **(b)** Behavior observed for an intrinsic emissivity of 0.1. Unlike the case of a nearly black fin (Fig. 2a), the heat transfer and efficiency of reflective panels vary over a relatively small actuation angle range ($\phi \lesssim 60°$).

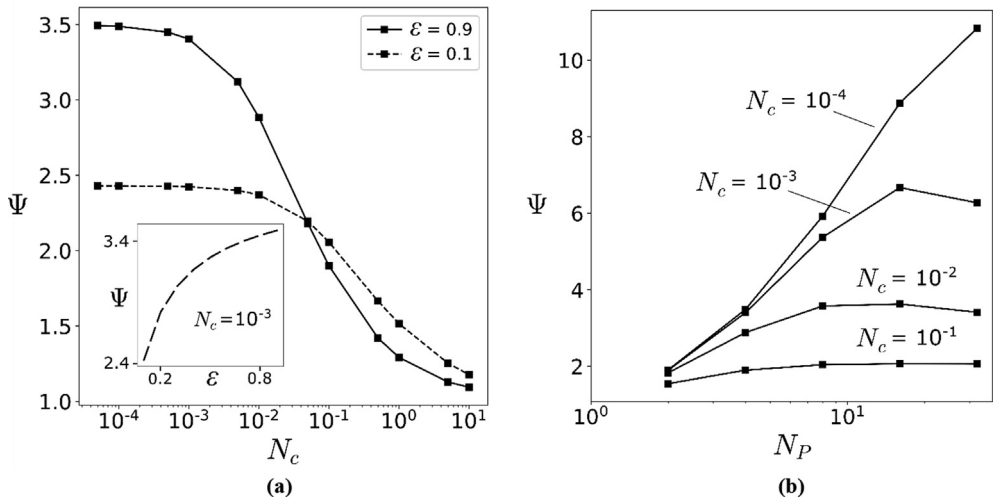

Fig. 5. (a) Turn-down ratio (Ψ) of a dynamic fin with four panels as a function of the conduction-radiation interaction parameter (N_c) for two different values of intrinsic emissivity. Black fins achieve larger possible turn-down ratios than reflective fins, although this is a function of N_c. The inset of the figure displays the variation of turn-down ratio as a function of emissivity for $N_c = 10^{-3}$. **(b)** Turn-down ratio (Ψ) of a nearly-black, dynamic fin as a function of the number of panels (N_P) considering four different values of the conduction-radiation interaction parameter (N_c).

hinges are relatively small compared with the temperature change due to conduction along the fin panels. However, as $N\kappa$ grows larger compared to N_c the temperature differential across the hinges grows in magnitude while the temperature profile along the panel length flattens until nearly isothermal. For the $N\kappa = 10$ curve in Fig. 6a, the temperature drop along the length of the first panel is only 0.01% of the total temperature drop along the entirety of the fin. As seen from Eq. (11), the temperature drop across a hinge is proportional to the rate of heat conduction through that hinge. At small angles ($\phi = 5°$), the temperature drop across each hinge is relatively constant, indicating that very little heat is lost by radiation into the surroundings from panels 2 and 3. However, as the radiator actuates towards an open position ($\phi = 150°$) the temperature drop across each hinge decreases along the length of the fin, indicating that panels 2 and 3 have a greater contribution to the total heat loss of the fin. Regarding emissivity, results are similar to the case of a large hinge conductance ($N\kappa = \Delta\chi N_c$), where temperature profiles for reflective surfaces show smaller temperature differences between fin base and fin tip. Likewise, the temperature drop across the thermal hinges are smaller for reflective surfaces. It should be noted that the non-dimensional temperature of the first element on the first panel is no longer equivalent to unity due to the presence of a thermal hinge between the first panel and the isothermal base.

When radiation dominates conduction ($N_c = 10$), the thermal hinges have little impact on the fin's temperature profile. If $N\kappa$ and N_c are on the same order, then the temperature profile is indistinguishable from the $N\kappa = \Delta\chi N_c$ scenario. As $N\kappa$ increases in value relative to N_c, the temperature profile experiences an overall decrease in value and the temperature difference between the first element and last element decreases in magnitude. The temperature drop across the thermal hinges likewise grow in magnitude as $N\kappa$ increases in value relative to N_c.

Concerning heat transfer and efficiency, increasing values of $N\kappa$ exacerbates the total heat transfer resistance of the fin, decreasing the heat transfer and fin efficiency when compared with values

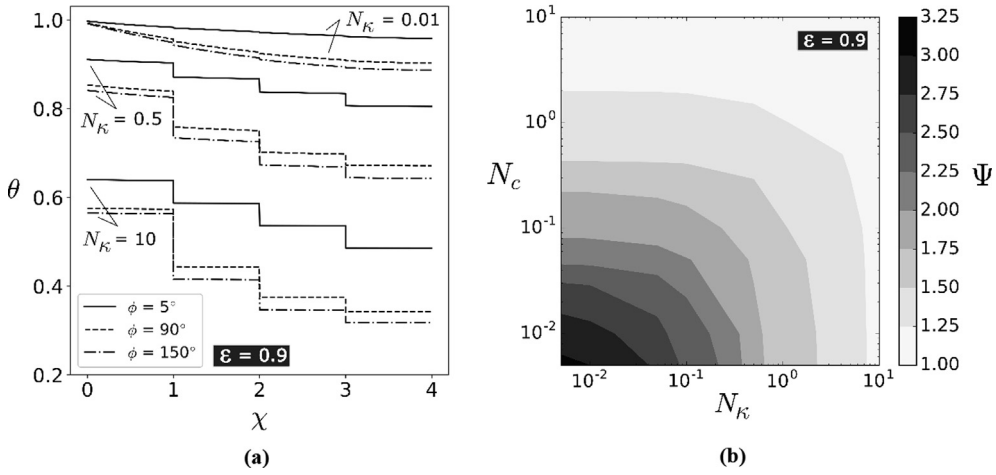

Fig. 6. (a) Non-dimensional temperature (θ) profiles as a function of non-dimensional panel position (χ) for an intrinsic emissivity of 0.9 and a conduction-radiation interaction parameter (N_c) of 0.01. Results are displayed for three different values of the hinge-conductance radiation parameter ($N\kappa$) and for increasing values of the actuation angle (ϕ), showing the influence of thermal hinge conductance and fin deployment position on the temperature profile. When N_c and $N\kappa$ are on the same order the influence of the hinge on the temperature profile is almost negligible. A large value for $N\kappa$ (relative to N_c) results in a significant temperature drop across the hinges and nearly isothermal temperatures along the panels. **(b)** Turn-down ratio (Ψ) of a nearly black dynamic fin as a function of N_c and $N\kappa$. Overall, N_c has a stronger influence on the turn-down ratio than $N\kappa$.

where $N\kappa = \Delta\chi N_c$. The largest decrease in heat transfer and efficiency occurs between $N\kappa$ values of 0.1 and unity, with the fully extended heat transfer decreasing by a relative difference of 64%. As with the case for infinite hinge thermal conductance, the change in fin efficiency with actuation is greatest for an intermediate value between the extremes of $N\kappa = 0.01$ and $N\kappa = 10$.

Fig. 6b displays the influence of both N_c and $N\kappa$ on the turn-down ratio of the device for a nearly black fin ($\varepsilon = 0.9$). Increasing either N_c or $N\kappa$ results in a decreased turn-down capability; however, N_c has a greater influence on the turn-down ratio value as compared to $N\kappa$.

3.4. Application and design considerations

Fundamental design considerations regarding the use of dynamic fins are similar to those suggested for straight radiative fins. Specifically, fins with larger N_c values (e.g. short, thick fins constructed from a thermally-conductive material) are more efficient and achieve greater heat transfer values than fins with lower N_c values. Likewise, a low-emissivity fin experiences much lower heat transfer rates but exhibits higher fin efficiencies as compared to a black fin. Several points of discussion concerning the influence of self-irradiation, actuation, and thermal hinge losses on the radiative heat transfer behavior of a dynamic fin are now provided.

First, and most noteworthy, dynamic fins are capable of turn-down ratios on the order of three or greater (Fig. 5a and 5b). A turn-down ratio of ~3 is on the order of turn-down ratios available by switching coatings or other devices currently under development [39–43]. However, the current approach using a radiative, segmented fin can utilize common materials and realistic fin dimensions. For example, a turn-down ratio of three is achievable with a dynamic fin comprised of four black panels ($L = 0.1$ m and $t = 0.005$ m) constructed from pure aluminum, coated with a nearly black coating ($\varepsilon = 0.9$) and connected to a base held at 293 K. The use of shorter or thicker panels or the use of materials with higher conductivities (such as copper or aluminum with integrated heat pipes) would further increase the turn-down ratio. Therefore, dynamic fins could prove useful in practical applications.

From a design perspective, an effective dynamic fin should utilize high thermal conductivity materials, thermal hinges with very low thermal resistance, and nearly-black surface coatings. These conditions would minimize the mass of the system while allowing for maximum total heat transfer and the largest possible turn-down ratio. The number of panels as well as the thickness and length of the panels may be tailored to the geometry of the application, although care must be taken in the correct selection of L and N_P. The turn-down ratio is maximized by increasing the deployed surface area and decreasing the N_c value until it is sufficiently small. Increases in deployed surface area are possible both by increasing the length of the fin (L) and/or by increasing the number of panels (N_P). However, increasing the length of the panels also increases N_c substantially, decreasing the turn-down ratio. This appears to suggest that adding panels is advantageous when compared with increasing the panel length, but the presence of the thermal hinge must be considered. Since N_c has a more significant impact than $N\kappa$ on the fin's turn-down ratio potential (as shown in Fig. 6b), the length of the panels should first be increased until the value of N_c is less than $N\kappa$. Once this condition is satisfied, the number of panels may be increased. However, as shown in Fig. 5b, the number of panels cannot be increased indefinitely (for a given N_c), as there is an optimum number of panels to achieve the maximum turn-down ratio for any given N_c value.

Second, radiative exchange between panels universally decreases the turn-down ratio potential of a dynamic fin. For the case of a black fin where conduction dominates ($N_c < 1$), radiation exchange between panels for small angles provides an additional path by which energy is transferred along the panels. This inter-panel radiative exchange increases the total heat transfer at the lowest angles which in turn decreases the turn-down ratio of the device. Likewise, for a black fin where radiation dominates ($N_c > 1$), inter-panel radiative exchange is even more significant and penalizes the fin by reversing the direction of heat transfer via conduction entirely (as shown in Fig. 3b), causing the heat transfer to remain almost unchanged for the entire actuation range (as shown in Fig. 4a). This suggests that the ideal variable geometry fin is a straight fin capable of varying its length in real time (all other properties remaining the same) which would obtain larger turn-down ratios than a folded fin of an equivalent fully deployed length.

Third, reflective fins have interesting behavior but do not make useful dynamic fins from a practical standpoint. For reflective fins where conduction dominates, radiative exchange between panels results in significant variation in heat transfer in the small actuation angles ($0° < \phi < 60°$). This results in a four-panel fin that is capable of a turn-down ratio of 2.5 where the fin has reached 90% of its full heat transfer potential at an actuation position of only 60°. This small actuation range indicates a fin that is capable of rapid heat transfer control through minimal geometric manipulation. However, the extremely low emissivity of the fin surfaces significantly reduces the total heat transfer capability of each panel, requiring the surface area (and mass) of the reflective fin to increase significantly in order to match the heat transfer from a black fin. Likewise, reflective fins cannot match the turn-down ratios achieved by a black fin.

Finally, panel geometry and material (N_c) have a larger negative impact on turn-down ratio than the heat transfer performance of the thermal hinge ($N\kappa$). If $N_c = 0$, the turn-down ratio is approximately 2.25 when $N\kappa = 0.1$ (Fig. 6b). However, for $N_c = 0.1$ and $N\kappa = \Delta\chi N_c$, the turn-down ratio is approximately 1.75. This behavior is true for all values of $N\kappa$ and N_c. This suggests, in application, that minimization of N_c should be prioritized over minimization of $N\kappa$.

With regards to future work, specular reflection should be incorporated into the model, allowing for a study of how this reflection mode impacts heat transfer behavior. Also, the model might be developed to work in three dimensions, allowing real tessellations to be explored to identify tessellations that optimize turn-down ratio and provide significant heat transfer control over the full range of actuation. Likewise, this work considered panels with uniform thickness and length. However, variations in the length, thickness, and emissivity of individual panels should be considered in optimizing the performance of self-irradiating, dynamic fins with regards to the heat transfer per unit mass of the system. The influence of external radiative inputs, including solar gains and emission/reflection from the radiative fin base structure, should be considered to more accurately depict the behavior of this device in specific applications. Finally, the use of coatings capable of emissivity variation (such as thermochromic or electrochromic coatings) on the surface of the dynamic fin should be modeled to explore the use of multiple radiative heat transfer variation mechanisms operating simultaneously.

4. Conclusion

A numerical algorithm was developed and used to explore the impact of heat conduction, self-irradiation, hinge thermal conductance, and panel emissivity on the overall performance of an actuating, accordion fin with adjustable geometry for dynamic control of radiating fins. Results show that dynamic fins are capable of turn-down ratios on the order of three or greater for realistic selections of panel geometry, panel material, and number of panels. Results have also shown that there exists an optimum number of panels such that turn-down ratio is maximized for a given panel

geometry and material. Also, inter-panel radiative exchange always acts to reduce the turn-down ratio of a folding fin by providing an additional pathway by which energy moves along the length of the fin. Regarding emissivity, reflective fins may be used to rapidly adjust the heat rate, but this rapid response comes at the cost of relatively low total heat rates. Finally, panel geometry and material selection have a more significant impact on radiator turn-down ratio than hinge construction and performance, suggesting that optimization of the panel performance should be preferred over optimization of the hinge performance.

Declaration of Competing Interest

None.

Acknowledgments

This material is based upon work supported by a NASA Space Technology Research Fellowship (grant number NNX15AP49H) and the National Science Foundation, United States (grant number 1749395).

Appendix A. Supplementary material

Supplementary data to this article can be found online at https://doi.org/10.1016/j.ijheatmasstransfer.2019.118441.

References

[1] D.G. Gilmore, Spacecraft Thermal Control Handbook, second ed., The Aerospace Corporation Press, El Segundo, CA, 2002.
[2] M.M. Hossain, M. Gu, Radiative cooling: principles, progress, and potentials, Adv. Sci. 3 (2016) 1–10, https://doi.org/10.1002/advs.201500360.
[3] Y. Zhai, Y. Ma, S.N. David, D. Zhao, R. Lou, G. Tan, R. Yang, X. Yin, Scalable-manufactured randomized glass-polymer hybrid metamaterial for daytime radiative cooling, Science 355 (2017) 1062–1066, https://doi.org/10.1126/science.aai7899.
[4] S. Fan, A. Raman, Metamaterials for radiative sky cooling, Natl. Sci. Rev. 5 (2018) 132–133, https://doi.org/10.1093/nsr/nwy012.
[5] S. Vall, A. Castell, Radiative cooling as low-grade energy source: a literature review, Renew. Sustain. Energy Rev. 77 (2017) 803–820, https://doi.org/10.1016/j.rser.2017.04.010.
[6] A.J. Juhasz, G.P. Peterson, Review of advanced radiator technologies for spacecraft power systems and space thermal control, NASA-TM-4555, NASA, Washington D.C., 1994. https://ntrs.nasa.gov/archive/nasa/casi.ntrs.nasa.gov/19940032314.pdf.
[7] H. Nagano, A. Ohnishi, Y. Nagasaka, Development of a lightweight deployable/stowable radiator for interplanetary exploration, Appl. Therm. Eng. 31 (2011) 3322–3331, https://doi.org/10.1016/j.applthermaleng.2011.06.012.
[8] R.B. Mulford, L.G. Christensen, M.R. Jones, B.D. Iverson, Dynamic control of radiative surface properties with origami-inspired design, J. Heat Transfer. 138 (2016) 32701, https://doi.org/10.1115/1.4031749.
[9] R.B. Mulford, V.H. Dwivedi, M.R. Jones, B.D. Iverson, Control of net radiative heat transfer with a variable emissivity accordion tessellation, J. Heat Transfer. 141 (2019), https://doi.org/10.1115/1.4042442 032702.
[10] B.D. Iverson, R.B. Mulford, E.T. Lee, M.R. Jones, Adaptive net radiative heat transfer and thermal management with origami-structured surfaces, in: Proceedings of the 16th International Heat Transfer Conference, Beijing, China, 2018, pp. 1–9.
[11] R.B. Mulford, N.S. Collins, M.S. Farnsworth, M.R. Jones, B.D. Iverson, Total hemispherical apparent radiative properties of the infinite V-groove with diffuse reflection, J. Thermophys. Heat Transf. 32 (2018) 1108–1112, https://doi.org/10.2514/1.T5485.
[12] R.B. Mulford, N.S. Collins, M.S. Farnsworth, M.R. Jones, B.D. Iverson, Total hemispherical apparent radiative properties of the infinite V-groove with specular reflection, Int. J. Heat Mass Transf. 124 (2018) p, https://doi.org/10.1016/j.ijheatmasstransfer.2018.03.041.
[13] C.K. Krishnaprakas, K. Badari Narayana, Heat transfer analysis of mutually irradiating fins, Int. J. Heat Mass Transf. 46 (2003) 761–769, https://doi.org/10.1016/S0017-9310(02)00356-3.
[14] B.V. Karlekar, B.T. Chao, Mass minimization of radiating trapezoidal fins with negligible base cylinder interaction, Int. J. Heat Mass Transf. 6 (1963) 33–48, https://doi.org/10.1016/0017-9310(63)90027-9.
[15] R.N. Krikkis, P. Razelos, On the optimizatin of circular radiating fins with fin to fin and fin to base radiant interaction, J. Heat Transf. 126 (2004) 134–137, https://doi.org/10.1115/1.1565094.
[16] R.N. Krikkis, P. Razelos, Optimum design of spacecraft radiators with longitudinal rectangular and triangular fins, J. Heat Transf. 124 (2002) 805, https://doi.org/10.1115/1.1497359.
[17] N. Ramesh, C. Balaji, S.P. Venkateshan, Numerical analysis of a cavity radiator with mutual interaction, Appl. Math. Model. 20 (1996) 476–484, https://doi.org/10.1016/0307-904X(95)00167-I.
[18] S.S. Kumar, N. Delhi, Optimized tubular radiator with annular fins on a nonisothermal base, Int. J. Heat Fluid Flow. 15 (1994) 399–410, https://doi.org/10.1016/0142-727X(94)90054-X.
[19] B.T.F. Chung, Optimization of radiating fin array including mutual irradiations between radiator elements, J. Heat Transf. 113 (1991) 814–822, doi: 10.115/1.2911208.
[20] D. Dannelley, J. Baker, Radiant fin performance using fractal-like geometries, J. Heat Transf. 135 (2013) 81902, https://doi.org/10.1115/1.4023883.
[21] M. Deiveegan, S.S. Katte, One-dimensional analysis of hollow conical radiating fins, J. Thermophys. Heat Transf. 18 (2003) 277–279, https://doi.org/10.2514/1.5847.
[22] M. Langer, M. Killian, D. Krejci, Thermal control of high power applications on cubesats p. IAC-18-C2.7.11, 69th International Astronautical Congress, IAF, Bremen, Germany, 2018.
[23] R.P. Reysa, R.L. Thurman, International space station environmental control and life support and thermal control systems overview, in: T.D. Guyenne (Ed.), Sixth European Symposium on Space Environmental Control Systems, European Space Agency, Noordwijk, The Netherlands, 1997, pp. 11–28.
[24] W.J. Krotiuk, C.J. Crowley, J.C. Rozzi, Propylene loop heat pipe with a lightweight, flexible, deployable radiator, AIP Conf. Proc. 608 (2002) 37–48, https://doi.org/10.1063/1.1449706.
[25] M. Amidieu, B. Moschetti, Development of a deployable radiator using a L.H.P as heat transfer element, in: T.D. Guyenne (Ed.), Sixth European Symposium on Space Environmental Control Systems, European Space Agency, Noordwijk, The Netherlands, 1997, pp. 283–288.
[26] V.L. Trujillo, E.S. Keddy, A. Merrigan, Michael, Design and demonstration of a high-temperature, deployable membrane heat pipe radiator element, in: W.D. Jackson (Ed.), Proceedings of the Intersociety Energy Conversion Engineering Conference, IEEE, Washington, D.C., 1989, pp. 1891–1895.
[27] R.B. Williams, G.S. Agnes, Lightweight deployable sunshade concepts for passive cooling for spacebased telescopes, in: Structures, Stuctural Dynamics, and Materials Conference, AIAA, Schaumburg, IL, 2008, pp. 1–16.
[28] H. Nagano, Y. Nagasaka, A. Ohnishi, Simple deployable radiator with autonomous thermal control function, J. Thermophys. Heat Transf. 20 (2006) 856–864, https://doi.org/10.1207/s15327752jpa8502.
[29] D.J. Hartl, J.B. Chong, P.P. Walgren, Demonstration of a shape memory alloy torque tube-based morphing radiator, in: A. Erturk, J.-H. Han (Eds.), Proc. SPIE, Active and Passive Smart Structures and Integrated Systems XII, SPIE, Denver, CO, 2018.
[30] M. Pesenti, G. Masera, F. Fiorito, M. Sauchelli, kinetic solar skin: a responsive folding technique, Energy Procedia 70 (2015) 661–672, https://doi.org/10.1016/j.egypro.2015.02.174.
[31] R.J. Lang, S. Magleby, L. Howell, Single degree-of-freedom rigidly foldable cut origami flashers, J. Mech. Robot. 8 (2016), https://doi.org/10.1115/1.4032102 031005.
[32] S.A. Zirbel, R.J. Lang, M.W. Thomson, D.A. Sigel, P.E. Walkemeyer, B.P. Trease, S. P. Magleby, L.L. Howell, Accommodating thickness in origami-based deployable arrays, J. Mech. Des. 135 (2013), https://doi.org/10.1115/1.4025372 111005.
[33] E.M. Sparrow, Effects of fin base temperature depression in a multifin array, J. Heat Transf. 97 (1975) 463–465.
[34] M.F. Modest, The Crossed-Strings Method, Radiative Heat Transfer, third ed., Academic Press, New York, NY, 2013, pp. 147–151.
[35] J.R. Howell, M.P. Menguc, Radiative transfer configuration factor catalog: a listing of relations for common geometries, J. Quant. Spectrosc. Radiat. Transf. 112 (2011) 910–912, https://doi.org/10.1016/j.jqsrt.2010.10.002.
[36] S.C. Chapra, R.P. Canale, Tridiagonal Systems, Numerical Methods for Engineers, sixth ed., McGraw-Hill, New York, NY, 2010, pp. 297–298.
[37] T.L. Bergman, A.S. Lavine, F.P. Incropera, D.P. DeWitt, Fundamentals of Heat and Mass Transfer, seventh ed., Wiley, Hoboken, NJ, 2011.
[38] J.R. Howell, R. Siegel, M.P. Menguc, Radiation Transfer with Conduction Boundary Conditions, Thermal Radiation Heat Transfer, fifth ed., CRC Press, Boca Raton, FL, 2011, pp. 342–350.
[39] S. Taylor, Y. Yang, L. Wang, Vanadium dioxide based Fabry-Perot emitter for dynamic radiative cooling applications, J. Quant. Spectrosc. Radiat. Transf. 197 (2017) 76–83, https://doi.org/10.1016/j.jqsrt.2017.01.014.
[40] R.L. Voti, G.L. Leahu, M.C. Larciprete, C. Sibilia, M. Bertolotti, Photothermal characterization of thermochromic materials for tunable thermal devices, Int. J. Thermophys. 36 (2015) 1004–1015, https://doi.org/10.1007/s10765-014-1790-2.
[41] H. Li, K. Xie, Y. Pan, H. Wang, H. Wang, Study of the mechanism of the variable emissivity infrared electrochromic device based on polyaniline conducting polymer, Synth. Met. 162 (2012) 22–25, https://doi.org/10.1016/j.synthmet.2011.11.002.
[42] A.L. Larsson, G.A. Niklasson, Infrared emittance modulation of all-thin-film electrochromic devices, Mater. Lett. 58 (2004) 2517–2520, https://doi.org/10.1016/j.matlet.2004.03.023.
[43] B.V. Bergeron, K.C. White, J.L. Boehme, A.H. Gelb, P.B. Joshi, Variable absorptance and emittance devices for thermal control, J. Phys. Chem. C 112 (2008) 832–838, https://doi.org/10.1021/jp076336d.